molecules

MDPI

Article

Interfacial Charge Transport Engineering in MoO_3 via Integration of PEDOT:PSS for Efficient and Durable Oxygen Evolution Reaction

Mrunal Bhosale * and Sahil Sanjay Magdum

School of Chemical Engineering, Yeungnam University, Gyeongsan 38541, Gyeongsanbuk-do, Republic of Korea
* Correspondence: mrunal.snst.1@gmail.com

Abstract

Electrochemical water oxidation is a grave half-reaction in overall water splitting. However, its practical efficiency is largely restricted by sluggish oxygen evolution reaction (OER) kinetics and the poor electrical conductivity of many transition-metal oxide catalysts. Herein, we report a rationally engineered molybdenum oxide-poly(3,4-ethylenedioxythiophene) (MoO_3-PEDOT:PSS) hybrid electrocatalyst designed to enhance interfacial charge transport and accelerate alkaline OER kinetics. The MoO_3 framework was first grown on carbon cloth through a hydrothermal route, accompanied by PEDOT:PSS surface modification using a simple immersion strategy. The conformal deposition of PEDOT:PSS onto molybdenum oxide nanostructures establishes a highly conductive and electronically coupled interface that significantly accelerates charge transport and optimizes adsorption energetics of reaction intermediates. Benefiting from the optimized integration of conductive PEDOT:PSS with the MoO_3 framework, the MoO_3-PEDOT:PSS-2 electrode delivers enhanced OER activity with a low overpotential of 302.4 mV at 10 mA cm^{-2}, a Tafel slope of 65.9 mV dec^{-1}, and stable performance after 5000 CV cycles and 30 h chronopotentiometry. In particular, the PEDOT:PSS layer not only facilitates efficient electron transport but also stabilizes the reconstructed active phases during prolonged operation, thereby suppressing performance degradation. This work highlights the critical role of polymer-assisted interfacial electronic modulation in transition metal oxides and provides a versatile strategy for designing next-generation, binder-free electrocatalysts for effectual and durable water oxidation.

Keywords: oxygen evolution reaction; conductive polymer interface; MoO_3-PEDOT:PSS hybrid electrocatalyst; electrode–electrolyte interface; interfacial charge transport

Check for updates

Academic Editor: Jianjun Wang

Received: 16 September 2026
Revised: 16 October 2026
Accepted: 20 October 2026
Published: 22 October 2026

Copyright: © 2026 by the authors. Licensee MDPI, Basel, Switzerland. This article is an open access article distributed under the terms and conditions of the Creative Commons Attribution (CC BY) license.

1. Introduction

Due to the increasing energy demand worldwide as well as the grave environmental impacts of fossil fuel combustion, the progress of clean, efficient, and sustainable energy technologies has developed an important research topic for researchers. Hence, extensive endeavors have been put forward to develop systems based on renewable energy technologies capable of large-scale energy conversion and storage [1–3]. Within the area of electrochemical energy technologies, the oxygen evolution reaction (OER) and the hydrogen evolution reaction (HER) have been recognized as two fundamental and potential approaches toward clean energy conversion and storage especially in water splitting [4–6]. Anodic OER and cathodic HER are the key processes to produce hydrogen that has been identified as one of the clean and renewable energy carriers [7,8]. The oxygen evolution

reaction is a complex four-electron oxidation process that involves sluggish reaction kinetics and a high thermodynamic/kinetic energy barrier, which significantly limits the efficiency of overall water splitting [9]. Recently, transition-metal-based composite oxides are becoming highly attractive as cost-effective and earth-abundant candidates with tunable electronic properties and wide applications in water electrolysis [10,11], Li-ion batteries [12], solar cells and the like, due to their unique properties. Nevertheless, the total efficiency of water splitting is primarily limited by the poor kinetics of the OER. The OER requires a complex four-electron transfer process to produce one oxygen molecule, while HER involves only a two-electron transfer process, so the former is the rate-determining step of water electrolysis [13]. Therefore, the OER usually requires a significantly higher overpotential than the HER, restricting the commercial application of hydrogen production via electrochemical water splitting [14,15].

Noble-metal-based catalysts such as RuO_2 and IrO_2 display excellent OER activity; however, their high cost, scarceness, and limited long-term stability restrict their large-scale practical application [16–19]. As a result, transition-metal oxides, hydroxides [20], sulfides [21], phosphides [22], and molybdate-based materials have attracted significant attention as alternative OER catalysts [23]. Among them, molybdenum oxide (MoO_3) is a promising candidate owing to its multiple oxidation states, layered crystal structure, good chemical stability, and rich redox chemistry. The presence of Mo^{6+}/Mo^{5+} redox couples can facilitate surface charge transfer and promote electrochemical reactions [24–26]. $Co_3(PO_4)_2$-MoO_{3-x} for alkaline water/seawater splitting [27], ZIF67@MoO_3 NSs@NF composite for effective oxygen evolution reaction and overall water-splitting [28], IrO2/MoO_3 [29], MoO_3 patches into NiNS [30]. However, the practical OER performance of pristine MoO_3 is still limited by its poor electrical conductivity, restricted active-site exposure, and sluggish interfacial charge transport.

To overcome these limitations, coupling MoO_3 with conductive polymers is an effective strategy to improve its electrocatalytic activity. Conductive polymers can enhance electron transport, regulate surface morphology, and provide flexible interfacial pathways for charge transfer [31–33]. Among various conductive polymers, poly(3,4-ethylenedioxythiophene), commonly known as PEDOT:PSS, is particularly attractive because of its high electrical conductivity, excellent environmental stability, good adhesion, and favorable electrochemical properties [34,35]. For example, Zhang et al. reported that an rGO/PEDOT:PSS composite can serve as an efficient catalyst for the oxygen reduction reaction, where the incorporation of PEDOT:PSS enhanced the electrical conductivity of the composite and improved its resistance toward CO poisoning [36]. Bingyang Ma et al. developed an MXene@PEDOT composite as a highly efficient photoelectrocatalyst for water-splitting applications [37]. Baruah B et al. developed NiO composited with PEDOT:PSS and rGO bifunctional electrocatalyst for methanol oxidation and OER [38].

The incorporation of PEDOT:PSS with MoO_3 can create a synergistic hybrid structure in which MoO_3 provides abundant redox-active sites, while PEDOT:PSS acts as a conductive network that accelerates electron transfer and improves electrode/electrolyte interaction. In this work, we demonstrate the synthesis of MoO_3-PEDOT:PSS hybrid electrocatalysts (Figure 1) for the enhanced OER in an alkaline medium and investigate their electrochemical performance. The optimized MoO_3-PEDOT:PSS electrode showed a high OER performance than pure MoO_3 in terms of low overpotential of 302.4 mV, rapid Tafel slope of 65.9 mV.dec^{-1}, reduced charge-transfer resistance (R_{ct}) of 4.6 Ω, and an advanced electrochemically active surface area of 103.87 cm^2. These performances are attributed to synergistic interactions between MoO_3 and PEDOT:PSS, that can contribute to increasing the conductivity of PEDOT:PSS, enhancing the interfacial coupling and charge transport at the interface of the electrode and electrolyte.

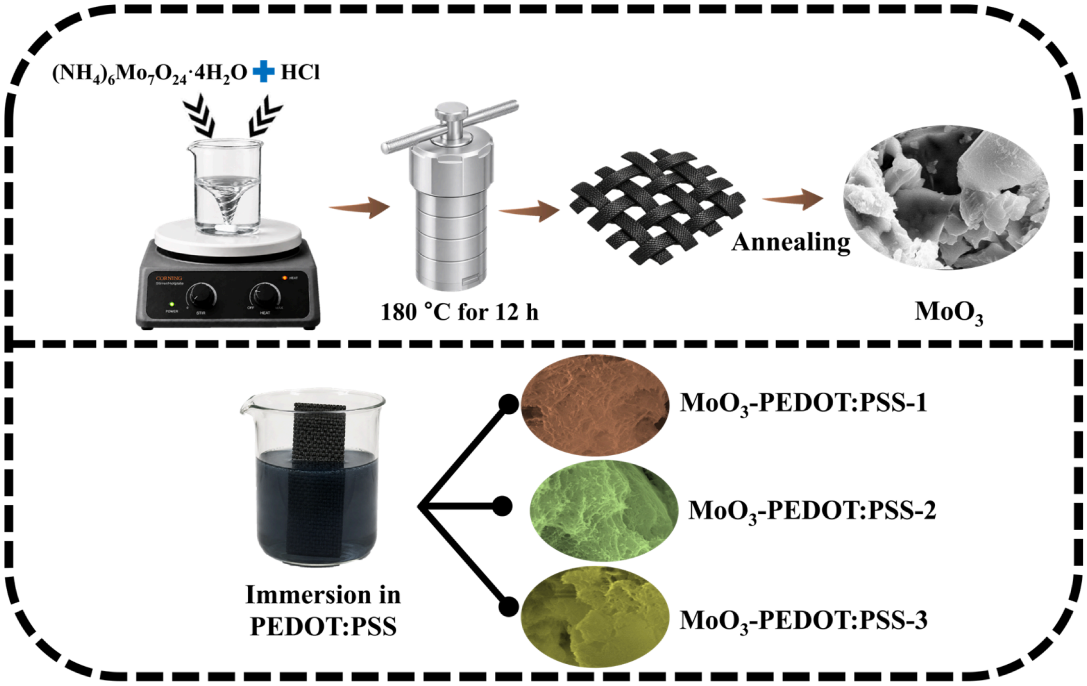


Figure 1. Schematic illustration of MoO_3-PEDOT:PSS synthesis.

2. Result and Discussion

The crystalline phase and structural evolution of MoO_3 and MoO_3-PEDOT:PSS composite electrodes were examined by X-ray diffraction (XRD), as exposed in Figure 2a. The XRD profiles recorded in the 2θ range of 10–70° display the characteristic diffraction features of MoO_3 along with the contribution from the carbon cloth substrate. For pristine MoO_3, the diffraction peaks situated at 2θ values of 17.6°, 20.7°, 23.0°, 28.7°, 29.9°, 33.8°, 34.9°, and 53.5° can be indexed to the (011), (110), (020), (−211), (111), (−222), (022), and (310) crystallographic planes of MoO_3, respectively, confirming the effective formation of the MoO_3 phase. These diffraction reflections are consistent with the standard JCPDS card No. 03-065-7675. The occurrence of distinct diffraction peaks directs the crystalline nature of the synthesized MoO_3 structure. In addition to the MoO_3-related reflections, broad diffraction bands centered around 24.9° and 42.4° are observed, which correspond to the (002) and (100) planes of carbon cloth, respectively. These peaks are in good agreement with JCPDS card No. 75-1621 [39]. After the introduction of PEDOT:PSS, the overall diffraction profile of MoO_3 is retained, suggesting that the PEDOT:PSS deposition does not destroy the primary crystalline framework of MoO_3. However, no additional sharp diffraction peaks related to PEDOT:PSS are detected in the MoO_3-PEDOT:PSS composites, indicating that PEDOT:PSS is mainly present in an amorphous or poorly crystalline state on the MoO_3 surface [40,41]. Notably, with increasing PEDOT:PSS incorporation, the intensity of the MoO_3 diffraction peaks gradually declines. This attenuation can be attributed to the progressive surface coverage of crystalline MoO_3 by the amorphous PEDOT:PSS layer, which weakens the diffraction signal originating from MoO_3. Meanwhile, the broad peak near 24–25° becomes more pronounced after PEDOT:PSS deposition, which may arise from the overlapping contribution of the carbon cloth substrate and the amorphous/conjugated polymeric structure of PEDOT:PSS. This observation further supports the successful formation of the MoO_3-PEDOT:PSS composite. The XRD results confirm the successful integration of amorphous PEDOT:PSS with crystalline MoO_3, forming a MoO_3-PEDOT:PSS composite structure while preserving the fundamental MoO_3 phase.

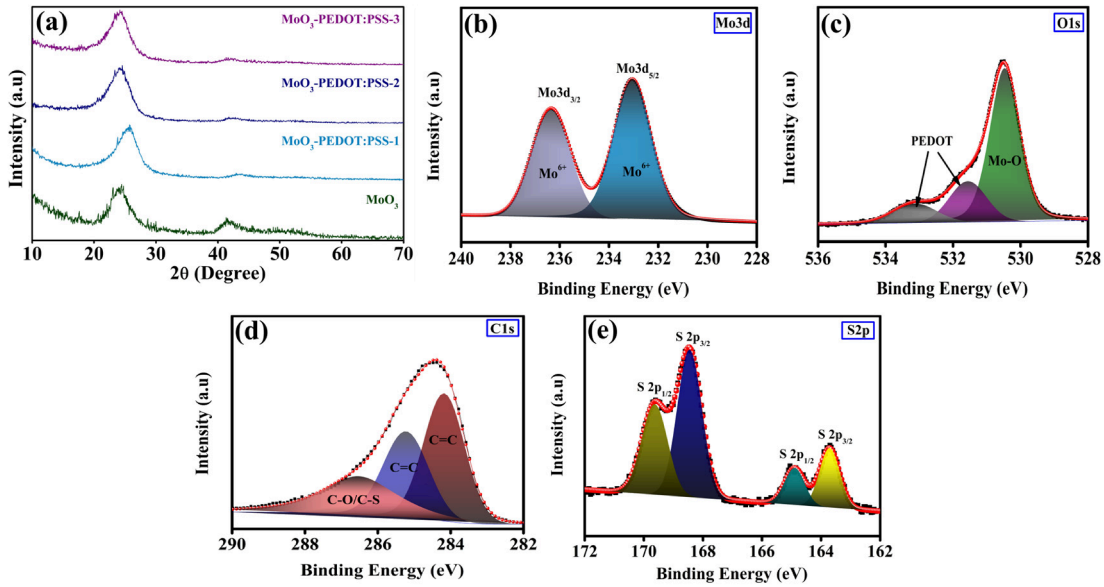


Figure 2. (**a**) XRD spectra of all the materials. High-resolution XPS spectra, (**b**) Mo 3d, (**c**) O 1s, (**d**) C 1s, and (**e**) S 2p spectra of MoO_3-PEDOT:PSS-2 composite.

X-ray photoelectron spectroscopy (XPS) was carried out to examine the surface chemical composition, and elemental valence states of the optimized MoO_3-PEDOT:PSS-2 composite. The high-resolution Mo 3d spectrum, shown in Figure 2b, displays two noticeable peaks located at binding energies of 233.1 and 236.3 eV. These peaks are allocated to Mo^{6+} $3d_{5/2}$ and Mo^{6+} $3d_{3/2}$, respectively, confirming the predominant presence of Mo in the +6-oxidation state within the MoO_3 framework [42,43]. The clear spin–orbit splitting of the Mo 3d doublet further verifies the successful formation of MoO_3 in the composite structure. The O 1s spectrum of MoO_3-PEDOT:PSS-2, presented in Figure 2c, was deconvoluted into three oxygen-related components. The peak positioned at 530.4 eV corresponds to lattice oxygen related with Mo-O bonding in MoO_3. The additional peaks situated at 531.5 and 533.2 eV can be ascribed to oxygen-containing functional groups associated with PEDOT:PSS [44–46]. Figure 2d presents the high-resolution C 1s spectrum of the MoO_3-PEDOT:PSS-2 composite. The deconvoluted peak at 284.1 eV is credited to the C=C bonding environment associated with the α-position carbon atoms of the thiophene ring, while the peak at 285.2 eV resembles to the C=C bonding of β-position carbon atoms in the PEDOT:PSS backbone. The additional peak located at 286.5 eV is allocated to C-O/C-S bonding, originating from the ethylenedioxy groups and thiophene units of PEDOT:PSS [47–49]. Furthermore, the high-resolution S 2p spectrum (Figure 2e) confirms the sulfur-containing thiophene structure of PEDOT and sulfonate structure in PSS chain. Two characteristic peaks located at 163.7 and 165.3 eV are assigned to S $2p_{3/2}$ and S $2p_{1/2}$, respectively, corresponding to sulfur atoms in the PEDOT:PSS backbone [37,50]. The additional peaks located at 168.4 and 169.6 eV can be assigned to the S $2p_{3/2}$ and S $2p_{1/2}$ spin–orbit components of sulfonate sulfur species in the PSS chain, respectively [49,51]. The appearance of these sulfur signals, along with the C 1s and O 1s contributions from PEDOT:PSS, confirms the successful deposition of PEDOT:PSS onto MoO_3.

The surface features and morphological development of the MoO_3 and MoO_3-PEDOT:PSS composite electrodes were examined using FESEM at various magnifications, as presented in Figure 3. The pristine MoO_3 sample, presented in Figure 3(a1–a3), displays a nanosheet-like morphology composed of irregularly stacked sheet structures. After the incorporation of PEDOT:PSS, noticeable changes in surface morphology are observed. For MoO_3-PEDOT:PSS-1, shown in Figure 3(b1–b3), the MoO_3 nanosheets are partially covered

by a thin polymeric layer with fiber-like features. This indicates the successful deposition of PEDOT:PSS on the MoO_3 surface. With further increase in PEDOT:PSS concentration, MoO_3-PEDOT:PSS-2 in Figure 3(c1–c3) displays a more uniform and interconnected polymeric network distributed over the MoO_3 nanosheet framework. The fiber-like PEDOT:PSS coating appears well integrated with the MoO_3 surface, forming an open and porous hybrid architecture. This optimized morphology is beneficial for exposing more electrochemically active sites, shortening ion-diffusion pathways, and enhancing electron transport through the conductive PEDOT:PSS network. In contrast, MoO_3-PEDOT:PSS-3, shown in Figure 3(d1–d3), exhibits a denser surface morphology due to excess PEDOT:PSS deposition. The higher PEDOT:PSS concentration appears to partially cover the MoO_3 nanosheet surface and reduce the openness of the electrode structure. Such excessive polymer coverage may block some active sites and restrict electrolyte diffusion, leading to less efficient ion/electron transport compared with MoO_3-PEDOT:PSS-2.

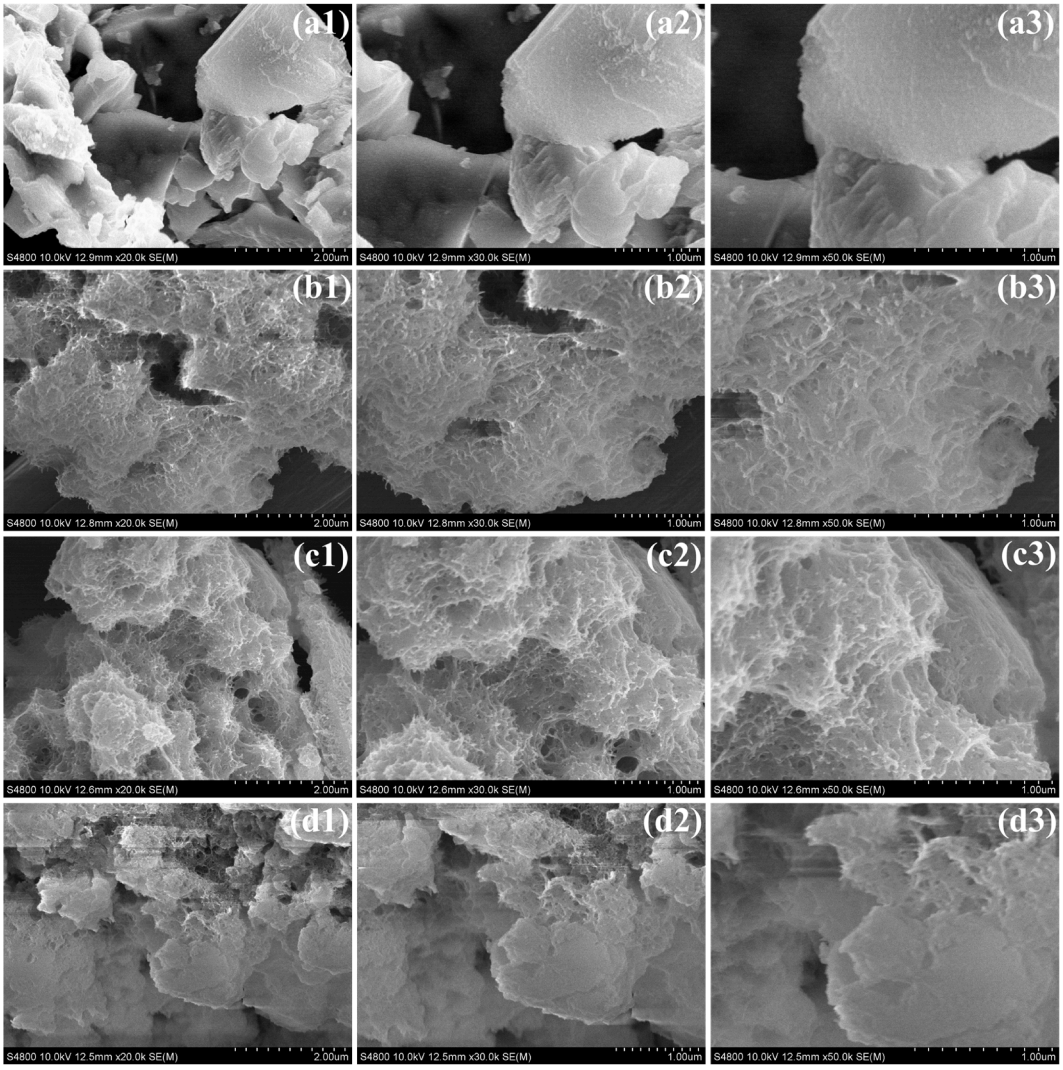


Figure 3. SEM micrograph images of (**a1**–**a3**) MoO_3, (**b1**–**b3**) MoO_3-PEDOT:PSS-1, (**c1**–**c3**) MoO_3-PEDOT:PSS-2, and (**d1**–**d3**) MoO_3-PEDOT:PSS-3.

Energy-dispersive X-ray spectroscopy (EDX) was conducted to determine the elemental composition and confirm the successful formation of MoO_3 and the MoO_3-PEDOT:PSS-2 composite, as revealed in Figure 4. The EDX spectrum of pristine MoO_3 (Figure 4(a1,a2)) shows the existence of Mo and O elements, with elemental contents of 48.28 wt% and 51.72 wt%, respectively. For the optimized MoO_3-PEDOT:PSS-2 composite, EDX spectrum

are presented in Figure 4(c1,c2). In addition to Mo and O, distinct C and S signals are observed, confirming the incorporation of PEDOT:PSS onto the MoO_3 surface. The elemental composition of MoO_3-PEDOT:PSS-2 was found to be 15.56 wt% Mo, 38.59 wt% O, 40.96 wt% C, and 4.89 wt% S. Elemental mapping was further performed to evaluate the localized distribution of the constituent elements. As shown in Figure 4(b1,b2), Mo and O are uniformly distributed throughout the pristine MoO_3 sample, indicating the homogeneous formation of the oxide structure. Similarly, the elemental mapping images of MoO_3-PEDOT:PSS-2 (Figure 4(d1–d4)) disclose an even distribution of Mo, O, C, and S across the selected region. The homogeneous dispersion of C and S confirms the effective coverage of PEDOT:PSS over the MoO_3 framework. Moreover, the uniform coexistence of Mo and PEDOT:PSS-related elements suggests strong interfacial contact between the crystalline MoO_3 nanosheets and the conductive polymeric PEDOT:PSS network.

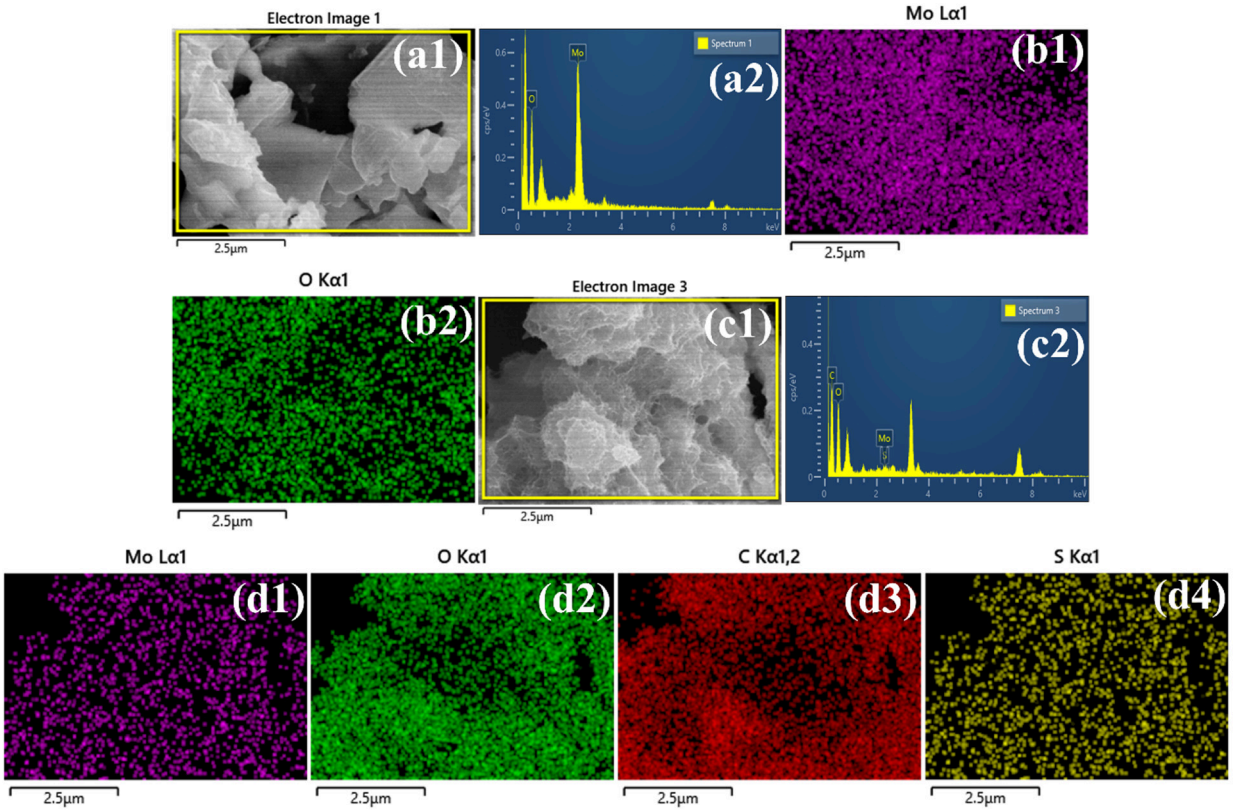


Figure 4. (**a1**,**a2**) EDX analysis, and (**b1**,**b2**) elemental mapping data of MoO_3. (**c1**,**c2**) EDX analysis, and (**d1**–**d4**) elemental mapping data of MoO_3-PEDOT:PSS-2.

The oxygen evolution reaction (OER) activity of the prepared electrocatalysts was systematically evaluated in alkaline medium, where the overpotential vital to deliver a benchmark current density is a critical indicator of catalytic efficiency [52]. A lower overpotential reflects more favorable reaction energetics and enhanced catalytic activity. As shown in Figure 5a, all MoO_3-PEDOT:PSS composite electrodes exhibited improved OER activity compared with pristine MoO_3 and bare carbon cloth (CC), confirming the beneficial role of PEDOT:PSS incorporation. Among the investigated samples, MoO_3-PEDOT:PSS-2 delivered the best catalytic performance, demanding an overpotential of only 302.4 mV to achieve a current density of 10 mA cm^{-2}. This value is considerably lesser than those of pristine MoO_3 (327.1 mV), MoO_3-PEDOT:PSS-1 (317.9 mV), and MoO_3-PEDOT:PSS-3 (314.8 mV) under identical testing conditions. The bare CC electrode exhibited negligible OER activity and failed to achieve a current density of 10 mA cm^{-2} within the investigated potential range, indicating its limited catalytic contribution. The superior activity of MoO_3-

PEDOT:PSS-2 can be attributed to the optimized PEDOT:PSS content by forming a conductive network with MoO_3, which accelerates electron transfer and reduces charge-transfer resistance during OER. However, excessive PEDOT:PSS loading in MoO_3-PEDOT:PSS-3 may partially block active sites or hinder ion diffusion, resulting in a slight decrease in catalytic performance compared with MoO_3-PEDOT:PSS-2. To further understand the reaction kinetics, Tafel analysis was performed, as presented in Figure 5b. The calculated Tafel slopes for MoO_3, MoO_3-PEDOT:PSS-1, MoO_3-PEDOT:PSS-2, and MoO_3-PEDOT:PSS-3 were 96.5, 84.7, 65.9, and 75.6 mV dec^{-1}, respectively. The knowingly reduced Tafel slope of MoO_3-PEDOT:PSS-2 indicates faster OER kinetics and more effectual charge-transfer behavior at the electrode–electrolyte interface. This observation is reliable with the overpotential trend revealed in Figure 5c, further demonstrating the superior catalytic efficiency of the optimized composite electrode. The Tafel slope of 65.9 mV dec^{-1} suggests that the rate-determining step is likely associated with the transformation of adsorbed *O intermediates into *OOH species during the OER process [53]. To further evaluate the catalytic performance of the optimized MoO_3-PEDOT:PSS-2 electrode, its OER activity was compared with previously reported Mo-based and conductive-polymer-modified electrocatalysts, as summarized in Table 1. Electrochemical impedance spectroscopy (EIS) was performed to evaluate the interfacial charge-transfer behavior of the synthesized electrocatalysts under OER conditions, as illustrated in Figure 5d. The attained Nyquist plots were fitted using an appropriate equivalent circuit to quantitatively determine the charge-transfer resistance (R_{ct}). The fitted R_{ct} values for MoO_3, MoO_3-PEDOT:PSS-1, MoO_3-PEDOT:PSS-2, and MoO_3-PEDOT:PSS-3 were 15.4, 10.9, 4.6, and 7.3 Ω, respectively. Among all the electrodes, MoO_3-PEDOT:PSS-2 unveiled the lowest R_{ct} value, signifying the most favorable charge-transfer behavior at the electrode–electrolyte interface. This reduced resistance confirms that the improved integration of PEDOT:PSS efficiently improves the electrical conductivity of MoO_3 and accelerates electron transport during the OER process, thereby contributing to enhanced catalytic kinetics.

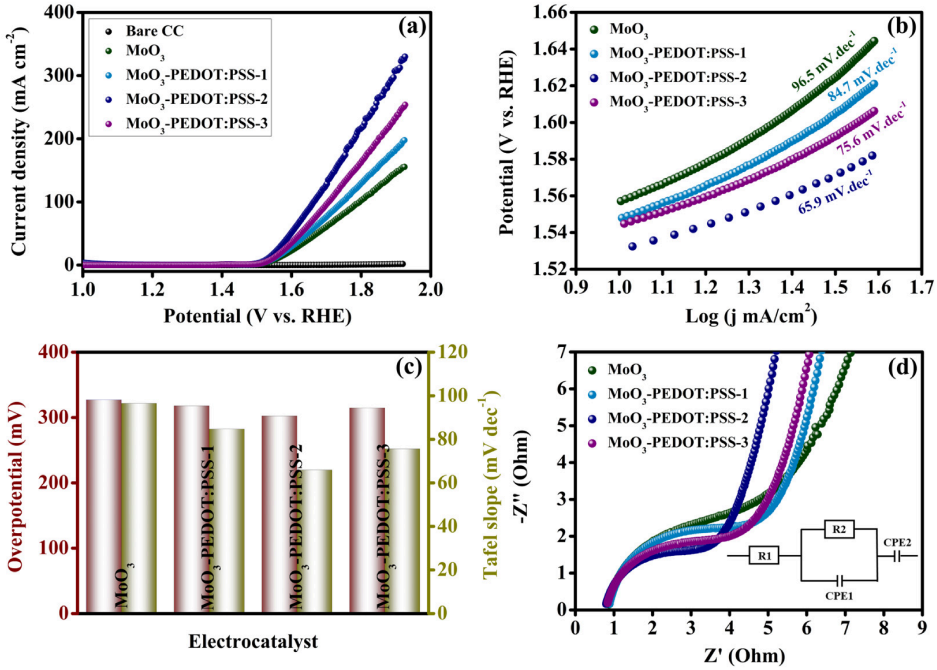


Figure 5. Electrochemical evaluation of the OER performance of the prepared electrocatalysts: (**a**) LSV curves recorded at a scan rate of 5 mV s^{-1}, (**b**) Tafel plots, (**c**) comparison of overpotential at 10 mA cm^{-2} and Tafel slope, and (**d**) EIS spectra with the fitted equivalent circuit shown in the inset.

Cyclic voltammetry measurements for MoO_3, MoO_3-PEDOT:PSS-1, MoO_3-PEDOT:PSS-2, and MoO_3-PEDOT:PSS-3 were conducted at various scan rates within the non-faradaic potential window, as presented in Figure 6a–d. In each case, the current density gradually increased with scan rate, indicating characteristic electrochemical double-layer capacitive behavior at the electrode/electrolyte boundary. To better correlate the OER activity with the availability of electrochemically accessible active sites, the electrochemically active surface area (ECSA) was determined using the double-layer capacitance (C_{dl}). The corresponding $2C_{dl}$ and C_{dl} values, shown in Figures 6e and 6f, respectively, were obtained from CV measurements recorded in the non-faradaic potential region. The estimated C_{dl} values for MoO_3, MoO_3-PEDOT:PSS-1, MoO_3-PEDOT:PSS-2, and MoO_3-PEDOT:PSS-3 were 2.93, 3.32, 4.15, and 3.65 mF cm^{-2}, respectively. Consistently, the corresponding ECSA values were determined to be 36.62, 83.12, 103.87, and 91.62 cm^2, respectively, as illustrated in Figure 6g. The highest C_{dl} and ECSA values obtained for MoO_3-PEDOT:PSS-2 indicate that this electrode possesses the largest number of electrochemically accessible active sites. The enhanced ECSA of MoO_3-PEDOT:PSS-2 can be attributed to the optimized PEDOT:PSS integration, which improves the electrode architecture by facilitating active-site exposure, strengthening interfacial contact, and promoting efficient ion/electron transport [54].

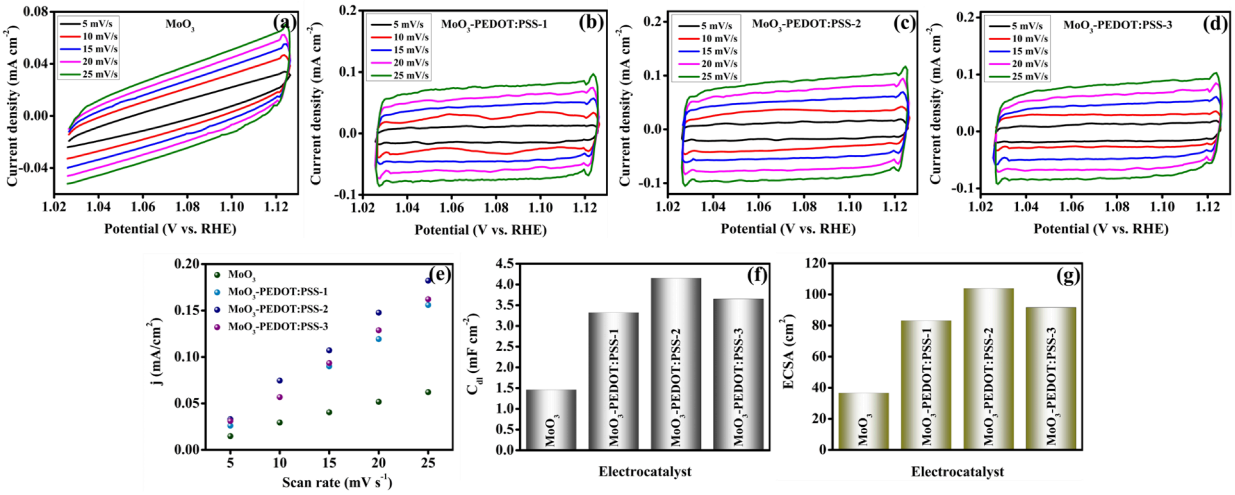


Figure 6. Cyclic voltammetry graph of (**a**) MoO_3, (**b**) MoO_3-PEDOT:PSS-1, (**c**) MoO_3-PEDOT:PSS-2, and (**d**) MoO_3-PEDOT:PSS-3 at diverse scan rate. (**e**) $2C_{dl}$ graph, (**f**) C_{dl} graph, and (**g**) ECSA outcomes of all the electrocatalyst.

The long-term operational stability of an electrocatalyst is a key criterion for evaluating its practical applicability in alkaline water oxidation. Therefore, the electrochemical durability of the augmented MoO_3-PEDOT:PSS-2 electrocatalyst was investigated in 1.0 M KOH using accelerated cyclic voltammetry and chronopotentiometry. The accelerated durability test was executed by continuous CV cycling at a scan rate of 50 mV s^{-1} to study the stability of the catalyst under repeated electrochemical oxidation circumstances. As revealed in Figure 7a, the LSV curves of MoO_3-PEDOT:PSS-2 were noted before and after 5000 CV cycles to evaluate the retention of OER activity. After prolonged cycling, the catalyst required an overpotential of 311.8 mV to sustain a current density of 10 mA cm^{-2}, showing only a slight increase compared with the initial value. This minimal change in overpotential indicates that the MoO_3-PEDOT:PSS-2 electrode maintains its catalytic activity and structural integrity during repeated OER operation. Although a noticeable decrease in current density is observed at higher applied potentials after 5000 CV cycles. This reduction may be associated with diminished accessibility or partial blockage of electrochemically active sites during prolonged electrochemical cycling. To further verify the

steady-state stability, chronopotentiometry was directed at a constant current density of 10 mA cm^{-2} for 30 h, as presented in Figure 7b. The MoO_3-PEDOT:PSS-2 electrocatalyst exhibited stable potential response over the continuous operation period, demonstrating good endurance under alkaline OER conditions. The slight performance fluctuation or minor loss observed during long-term operation may be associated with partial detachment or leaching of active species from the electrode surface, accumulation of generated oxygen bubbles at the electrode–electrolyte interface, and possible surface reconstruction or oxidation under high anodic potentials. Nevertheless, the overall stability results confirm that MoO_3-PEDOT:PSS-2 possesses robust electrochemical durability, making it a promising electrocatalyst for alkaline oxygen evolution [55,56]. The structural and morphological characteristics of the optimized MoO_3-PEDOT:PSS-2 electrode following the OER durability test were examined using XRD and FESEM analyses. As presented in Figure 7c, the post-stability XRD profile exhibits the principal diffraction features associated with MoO_3, suggesting that the crystalline phase is largely retained under the investigated electrochemical conditions. A reduction in diffraction peak intensity is observed after durability testing; however, no obvious additional crystalline phases are identified within the detection limits of the XRD measurement. Furthermore, the post-stability FESEM image in Figure 7d reveals that the electrode largely maintains its characteristic nanosheet-like morphology and interconnected surface features. Although localized surface roughening and partial aggregation are noticeable, the overall morphology remains recognizable after electrochemical testing.

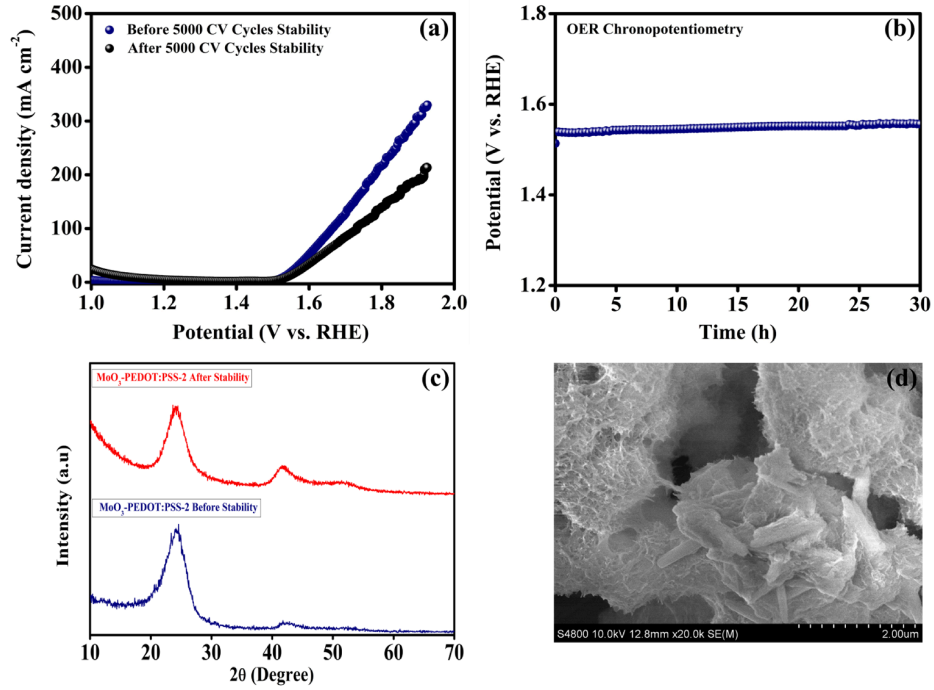


Figure 7. (**a**) LSV curves of MoO_3-PEDOT:PSS-2 before and after 5000 CV cycles and (**b**) chronopotentiometry analysis. After stability (**c**) XRD pattern, and (**d**) FESEM image of MoO_3-PEDOT:PSS-2.

Table 1. Comparison of present electrocatalyst OER performance result in 1 M KOH with other reported electrocatalysts.

Materials	Overpotential (mV)	Current Density	Ref.
Co-doped MoO_x	340	10 mA cm^{-2}	[57]
Ag doped MoO_3	330	10 mA cm^{-2}	[58]

Table 1. *Cont.*

Materials	Overpotential (mV)	Current Density	Ref.
$Cu(OH)_2$@MoO_3	308	10 mA cm^{-2}	[59]
MnO_x-MoO_3	390	10 mA cm^{-2}	[60]
$Co_2P_2O_7$@MoO_3/NF	377	10 mA cm^{-2}	[43]
Co-doped $MoSe_2$@PANI	385	10 mA cm^{-2}	[61]
Cu_2MoS_4-PANI/rGO	395	10 mA cm^{-2}	[62]
NiFeLDH@PANi-CF	310	10 mA cm^{-2}	[63]
$CoFe_2O_4$/PANI-MWCNTs	314	10 mA cm^{-2}	[64]
Fe-Mn@PANI/NF	353	10 mA cm^{-2}	[65]
$NiFe_2O_4$/Ni_3Fe/PANI	320	10 mA cm^{-2}	[66]
PPy/$ZnWO_4$	507	10 mA cm^{-2}	[67]
CoNiMn-LDH/PPy/RGO	369	10 mA cm^{-2}	[68]
PPy/IL nanoparticles	583	10 mA cm^{-2}	[69]
MoO_3-PEDOT:PSS-2	302	10 mA cm^{-2}	Present work

3. Experimental Section

3.1. Chemicals

Ammonium heptamolybdate tetrahydrate ($(NH_4)_6Mo_7O_{24}\cdot 4H_2O$) was purchased from Sigma-Aldrich (St. Louis, MO, USA). Hydrochloric acid (HCl, extra pure) and ethanol (C_2H_5OH, 94.5%) were obtained from Duksan Chemicals (Ansan-si, Gyeonggi-do, Republic of Korea). Potassium hydroxide (KOH, ≥85%) was provided by Daejung Chemicals & Metals (Siheung-si, Gyeonggi-do, Republic of Korea). A commercially available PEDOT:PSS aqueous dispersion (Clevios™ PH 1000, Lot No. 2015P0052) was obtained from Heraeus (Leverkusen, Germany). The dispersion contained 1.3 wt.% PEDOT:PSS solids, with a PSS-to-PEDOT weight ratio of approximately 2.5:1. High-purity carbon cloth (CC), used as the conductive scaffold and current collector for electrode preparation, was purchased from NARA Cell-Tech Corporation (Seoul, Republic of Korea). All reagents used in this study were analytical-grade chemicals and were utilized directly without any additional purification.

3.2. Preparation of MoO_3 and MoO_3-PEDOT:PSS

The synthesis process of MoO_3-PEDOT:PSS is illustrated in Figure 1. MoO_3 was synthesized directly on carbon cloth by a hydrothermal method. In a representative synthesis, 1.4 g of ($(NH_4)_6Mo_7O_{24}\cdot 4H_2O$) was added to 30 mL of deionized water and magnetically stirred for 20–30 min until a transparent and uniform solution was formed. Next, diluted HCl was introduced drop by drop to adjust the pH of the precursor solution to about 1–2. The acidic environment promotes the transformation of molybdate ions into molybdenum oxide or hydrated molybdenum oxide species during the hydrothermal reaction. The resulting solution was then transferred into a 50 mL Teflon-lined stainless-steel autoclave, and the pre-cleaned carbon cloth was vertically placed inside the Teflon liner, ensuring complete immersion in the precursor solution. The sealed autoclave was maintained at 180 °C for 12 h to complete the hydrothermal reaction. Following natural cooling to room temperature, the MoO_3-coated carbon cloth was carefully removed and washed numerous times with deionized water and ethanol to disregard residual ions and loosely attached particles. The obtained sample was dried at 60 °C for 8–12 h and subsequently annealed in air at 350 °C for 2 h to obtain the final MoO_3 electrode.

The MoO_3-PEDOT:PSS composite electrodes were prepared by a simple immersion method. The as-synthesized MoO_3-coated carbon cloth electrodes were individually im-

mersed for 2 min in PEDOT:PSS modification solutions prepared by dispersing 0.05, 0.10, and 0.15 g of the as-received commercial PEDOT:PSS aqueous dispersion in 30 mL of ultrapure water, respectively. After immersion, the electrode was slowly withdrawn from the PEDOT:PSS dispersion, allowed to drain naturally to remove excess solution, and dried at 60 °C for 6 h to obtain PEDOT:PSS-modified MoO_3. By varying the PEDOT:PSS concentration in the dispersion, different composite electrodes were obtained and denoted as MoO_3-PEDOT:PSS-1, MoO_3-PEDOT:PSS-2, and MoO_3-PEDOT:PSS-3.

3.3. Material Characterization

The structural, chemical, and morphological assets of the synthesized materials were systematically characterized using advanced analytical techniques. X-ray diffraction (XRD) analysis was achieved on an X'Pert Pro diffractometer by means of Cu Kα radiation (λ = 1.5418 Å) to detect the crystalline phases, evaluate phase purity, and examine the structural characteristics of the prepared samples. X-ray photoelectron spectroscopy (XPS) was implemented using a Thermo Scientific K-Alpha spectrometer to examine the surface elemental composition, oxidation states, and chemical bonding environments. The surface morphology and microstructural structures were analyzed by field-emission scanning electron microscopy (FESEM, HITACHI S-4800). Moreover, energy-dispersive X-ray spectroscopy (EDX) coupled with FESEM was employed to regulate the elemental composition and spatial distribution of the integral elements within the synthesized materials.

3.4. Electrochemical Analysis

Electrochemical analyses were performed at room temperature on a Bio-Logic VSP-300 electrochemical workstation (Gières, France) using a standard three-electrode system in 1.0 M KOH electrolyte. The synthesized catalyst materials were grown directly on carbon cloth, which was used as the working electrode. An Hg/HgO electrode and a platinum plate were used as the reference and counter electrodes, respectively. Before catalyst preparation, the carbon cloth was thoroughly treated by ultrasonication in 1.0 M HCl, deionized water, and ethanol for 20 min individually to eliminate exterior impurities, subsequently dried overnight at 60 °C.

The OER performance of the fabricated electrodes was examined using LSV at a scan rate of 5 mV s^{-1}. The recorded potentials were converted to the reversible hydrogen electrode (RHE) scale to enable reliable comparison of catalytic performance.

$$E_{RHE} = E_{Hg/HgO} + E^{\circ}{}_{Hg/HgO} + 0.0591 \times (pH) \quad (1)$$

where $E^{\circ}{}_{Hg/HgO}$ signifies the standard potential of the Hg/HgO reference electrode under alkaline conditions (pH ≈ 14). The Tafel slopes were determined by linear regression of the overpotential versus logarithmic current density (η-log j) plots within the current density range of 10–40 mA cm^{-2}. The electrochemical double-layer capacitance (C_{dl}) was determined from cyclic voltammetry (CV) curves recorded in the non-Faradaic potential area of 0.1–0.2 V vs. Hg/HgO at different scan rates ranging from 5 to 25 mV s^{-1}. The electrochemically active surface area (ECSA) was assessed from the obtained C_{dl} results using a specific capacitance (C_s) of 0.040 mF cm^{-2} conferring to the following equation:

$$ECSA = Cdl/Cs \quad (2)$$

Electrochemical impedance spectroscopy (EIS) was performed at an applied potential of 1.53 V over a frequency of 100 kHz to 0.1 Hz with an AC amplitude of 10 mV. The electrochemical resilience of the augmented electrocatalyst was assessed by accelerated cycling stability tests involving 5000 continuous CV cycles at a scan rate of 50 mV s^{-1}. The LSV

polarization curves verified before and after cycling were compared to evaluate activity retention. In addition, long-term operational stability was inspected by chronopotentiometry at a constant current density under continuous OER conditions.

4. Conclusions

In summary, a MoO_3-PEDOT:PSS hybrid electrocatalyst was successfully developed on carbon cloth through hydrothermal growth of MoO_3 followed by PEDOT:PSS surface modification using a simple immersion strategy. The structural and surface analyses confirmed the formation of crystalline MoO_3 and the successful incorporation of PEDOT:PSS, where the conductive polymeric network effectively modified the MoO_3 surface without disturbing its primary crystalline framework. Among the prepared electrodes, MoO_3-PEDOT:PSS-2 exhibited the most favorable morphology, with an optimized nanosheet-polymeric-network architecture that promoted active-site exposure, electrolyte accessibility, and interfacial charge transport. The optimized MoO_3-PEDOT:PSS-2 electrode delivered superior alkaline OER performance, requiring a low overpotential of 302.4 mV to achieve 10 mA cm^{-2}, which was knowingly lower than those of pristine MoO_3 (327.1 mV), MoO_3-PEDOT:PSS-1 (317.9 mV), and MoO_3-PEDOT:PSS-3 (314.8 mV). In addition, MoO_3-PEDOT:PSS-2 exhibited the smallest Tafel slope of 65.9 mV dec^{-1}, confirming faster OER kinetics. The enhanced catalytic activity was further supported by its reduced R_{ct} of 4.6 Ω, higher C_{dl} value of 4.15 mF cm^{-2}, and enlarged ECSA of 103.87 cm^2, demonstrating improved electrochemical accessibility and effective electron transport at the electrode–electrolyte interface. Furthermore, MoO_3-PEDOT:PSS-2 shows reasonable activity after 5000 CV cycles, with an overpotential of 311.8 mV at 10 mA cm^{-2}, and preserved stable operation during 30 h chronopotentiometry testing. The improved OER performance of MoO_3-PEDOT:PSS-2 may be associated with the beneficial integration of MoO_3 and conductive PEDOT:PSS, which facilitates interfacial charge transport, electrochemical accessibility, and favorable reaction kinetics.

Author Contributions: M.B.: Conceptualization, methodology, investigation, writing—original draft, software, visualization; S.S.M.: formal analysis, review and editing. All authors have read and agreed to the published version of the manuscript.

Funding: This research received no external funding.

Data Availability Statement: The data presented in this study are available on request from the corresponding author. (please specify the reason for restriction, e.g., the data are not publicly available due to privacy or ethical restrictions.)

Conflicts of Interest: The authors declare no conflicts of interest.

References

1. Dresselhaus, M.S.; Thomas, I. Alternative energy technologies. *Nature* **2001**, *414*, 332–337. [CrossRef] [PubMed]
2. Zhao, Y.; Nakamura, R.; Kamiya, K.; Nakanishi, S.; Hashimoto, K. Nitrogen-doped carbon nanomaterials as non-metal electrocatalysts for water oxidation. *Nat. Commun.* **2013**, *4*, 2390. [CrossRef] [PubMed]
3. He, X.; Li, Z.; Yao, Y.; Luo, F.; Sun, X.; Tang, B. Surface and interfacial engineering of electrocatalysts for seawater electrolysis. *Acc. Chem. Res.* **2026**, *59*, 518–528. [CrossRef] [PubMed]
4. Aghamohammadi, P.; Hüner, B.; Altıncı, O.C.; Akgul, E.T.; Teymur, B.; Simsek, U.B.; Demir, M. Recent advances in the electrocatalytic applications (HER, OER, ORR, water splitting) of transition metal borides (MBenes) materials. *Int. J. Hydrogen Energy* **2024**, *87*, 179–198. [CrossRef]
5. He, R.; Sun, Q.; Thangasamy, P.; Chen, X.; Zhang, Y.; Wang, H.; Luo, H.; Zhou, X.-D.; Zhou, M. Accelerate oxygen evolution reaction by adding chemical mediator and utilizing solar energy. *Int. J. Hydrogen Energy* **2023**, *48*, 8898–8908. [CrossRef]
6. He, J.; He, Y.; Liu, X.; Sun, H.; Mao, H.; Yang, D.; Li, M.; Zhou, S.; Zhao, Y. Beyond oxygen evolution: Recent progress in hydrogen production via anodic substitution reactions. *Mater. Rep. Energy* **2026**, *6*, 100426. [CrossRef]

7. Irshad, H.; Zia, M.; Al-Hajri, R.; Khattak, Z.A.; Al-Abri, M.; Ahmad, N.; Younus, H.A. Electrocatalysts for hydrogen and oxygen evolution reactions under neutral/near-neutral conditions: Summary and challenges. *Int. J. Hydrogen Energy* **2025**, *137*, 1009–1041. [CrossRef]
8. Eikeng, E.; Makhsoos, A.; Pollet, B.G. Critical and strategic raw materials for electrolysers, fuel cells, metal hydrides and hydrogen separation technologies. *Int. J. Hydrogen Energy* **2024**, *71*, 433–464. [CrossRef]
9. Abdelghafar, F.; Xu, X.; Jiang, S.P.; Shao, Z. Perovskite for electrocatalytic oxygen evolution at elevated temperatures. *ChemSusChem* **2024**, *17*, e202301534. [CrossRef] [PubMed]
10. Rathika, A.; Peter, I.J.; Nithiananthi, P. Synergistic MnMo2S4 and reduced graphene oxide nanocomposite: A catalyst for efficient energy storage and water electrolysis. *J. Power Sources* **2025**, *649*, 237433. [CrossRef]
11. Kamaruzaman, N.A.; Khairul, W.M.; Saleh, N.M.; Yusoff, F. Advancements in carbon-based transition metal compounds for enhanced hydrogen production via electrochemical water splitting. *Int. J. Electrochem. Sci.* **2024**, *19*, 100740. [CrossRef]
12. Fagiolari, L.; Sampò, M.; Lamberti, A.; Amici, J.; Francia, C.; Bodoardo, S.; Bella, F. Integrated energy conversion and storage devices: Interfacing solar cells, batteries and supercapacitors. *Energy Storage Mater.* **2022**, *51*, 400–434. [CrossRef]
13. Plevova, M.; Hnat, J.; Bouzek, K. Electrocatalysts for the oxygen evolution reaction in alkaline and neutral media. A comparative review. *J. Power Sources* **2021**, *507*, 230072. [CrossRef]
14. Raveendran, A.; Chandran, M.; Dhanusuraman, R. A comprehensive review on the electrochemical parameters and recent material development of electrochemical water splitting electrocatalysts. *RSC Adv.* **2023**, *13*, 3843–3876. [CrossRef] [PubMed]
15. Sahin, N.E.; Pech-Rodríguez, W.; Meléndez-González, P.; Lopez Hernández, J.; Rocha-Rangel, E. Water splitting as an alternative for electrochemical hydrogen and oxygen generation: Current status, trends, and challenges. *Energies* **2023**, *16*, 5078. [CrossRef]
16. Wei, J.; Zhou, M.; Long, A.; Xue, Y.; Liao, H.; Wei, C.; Xu, Z.J. Heterostructured electrocatalysts for hydrogen evolution reaction under alkaline conditions. *Nano-Micro Lett.* **2018**, *10*, 75. [CrossRef] [PubMed]
17. Chen, J.; Chen, C.; Qin, M.; Li, B.; Lin, B.; Mao, Q.; Yang, H.; Liu, B.; Wang, Y. Reversible hydrogen spillover in Ru-WO3-x enhances hydrogen evolution activity in neutral pH water splitting. *Nat. Commun.* **2022**, *13*, 5382. [CrossRef] [PubMed]
18. Zhou, L.; Yu, J.; Wei, D.; Shi, C.; Jin, H.; Li, H.; Zhu, E.; Xu, M. Electronic structure engineering of Fe-NC catalysts by proximity electronic effect of S ligand for enhanced oxygen electrocatalysis. *Carbon Neutr. Syst.* **2025**, *1*, 18. [CrossRef]
19. Khrizanforov, M.N.; Samorodnova, A.P.; Bezkishko, I.A.; Gainullin, R.R.; Kholin, K.V.; Gubaidullin, A.T.; Shekurov, R.P.; Miluykov, V.A. 2D coordination polymers of transition metals as catalysts for oxygen evolution reaction. *Mater. Rep. Energy* **2025**, *5*, 100334. [CrossRef]
20. Zhang, Z.; Li, X.; Zhong, C.; Zhao, N.; Deng, Y.; Han, X.; Hu, W. Spontaneous synthesis of silver-nanoparticle-decorated transition-metal hydroxides for enhanced oxygen evolution reaction. *Angew. Chem. Int. Ed.* **2020**, *59*, 7245–7250. [CrossRef] [PubMed]
21. Li, T.; Jiang, K.; Li, Y.; Luo, H.; Wang, Z.; Liu, Y.-Q. Crystalline nickel sulfide integrated with amorphous cobalt sulfide as an efficient bifunctional electrocatalyst for water splitting. *Int. J. Hydrogen Energy* **2023**, *48*, 7337–7345. [CrossRef]
22. Jiang, K.; Luo, M.; Peng, M.; Yu, Y.; Lu, Y.-R.; Chan, T.-S.; Liu, P.; de Groot, F.M.; Tan, Y. Dynamic active-site generation of atomic iridium stabilized on nanoporous metal phosphides for water oxidation. *Nat. Commun.* **2020**, *11*, 2701. [CrossRef] [PubMed]
23. Kim, K.-H.; Hong, D.; Kim, M.G.; Choi, W.; Min, T.; Kim, Y.-M.; Choi, Y.-H. Improving electrocatalytic activity of MoO_3 for the oxygen evolution reaction by incorporation of Li ions. *ACS Mater. Lett.* **2023**, *5*, 1196–1201. [CrossRef]
24. Chibane, L.; Belkaid, M.S.; Zirmi, R.; Moussi, A. A simple process for synthesis of transparent thin films of molybdenum trioxide in the orthorhombic phase (α-MoO_3). *J. Electron. Mater.* **2017**, *46*, 1963–1970. [CrossRef]
25. Avani, A.; Anila, E. Recent advances of MoO_3 based materials in energy catalysis: Applications in hydrogen evolution and oxygen evolution reactions. *Int. J. Hydrogen Energy* **2022**, *47*, 20475–20493. [CrossRef]
26. Reshak, A. Specific features of electronic structures and optical susceptibilities of molybdenum oxide. *RSC Adv.* **2015**, *5*, 22044–22052. [CrossRef]
27. Yang, M.; Shi, B.; Tang, Y.; Lu, H.; Wang, G.; Zhang, S.; Sarwar, M.T.; Tang, A.; Fu, L.; Wu, M. Interfacial chemical bond modulation of $Co_3(PO_4)_2$-MoO_{3-x} heterostructures for alkaline water/seawater splitting. *Inorg. Chem.* **2023**, *62*, 2838–2847. [CrossRef] [PubMed]
28. Wei, X.; Chai, Y.; Liu, N.; Qiao, S.; Fu, Y.; Chong, S. ZIF67@ MoO_3 NSs@ NF composite electrocatalysts reinforced by chemical bonds and oxygen vacancy for efficient oxygen evolution reaction and overall water-splitting. *Int. J. Hydrogen Energy* **2022**, *47*, 9606–9615. [CrossRef]
29. Tariq, M.; Zaman, W.Q.; Sun, W.; Zhou, Z.; Wu, Y.; Cao, L.-m.; Yang, J. Unraveling the beneficial electrochemistry of IrO_2/MoO_3 hybrid as a highly stable and efficient oxygen evolution reaction catalyst. *ACS Sustain. Chem. Eng.* **2018**, *6*, 4854–4862. [CrossRef]
30. Liu, Y.; Liu, P.; Men, Y.-L.; Li, Y.; Peng, C.; Xi, S.; Pan, Y.-X. Incorporating MoO_3 patches into a Ni oxyhydroxide nanosheet boosts the electrocatalytic oxygen evolution reaction. *ACS Appl. Mater. Interfaces* **2021**, *13*, 26064–26073. [CrossRef] [PubMed]
31. Nie, W.; Ruan, M.; Liu, X.; Ruan, K.; Sun, Y.; Liu, Z. Enhancing the photoelectrochemical hydrogen evolution activity of polyaniline through small molecular acid doping to introduce polariton-enhanced active sites. *Chem. Eng. J.* **2024**, *480*, 148321. [CrossRef]

32. Yang, R.; Shi, H.; Zhao, J.; Zhang, H.; Zhong, M.; Yang, P. Novel asymmetric aggregation strategy to boost charge separation in carbon nitride polymers for high-performance hydrogen photosynthesis. *ACS Catal.* **2024**, *14*, 9607–9617. [CrossRef]
33. Kayser, L.V.; Lipomi, D.J. Stretchable conductive polymers and composites based on PEDOT and PEDOT: PSS. *Adv. Mater.* **2019**, *31*, 1806133. [CrossRef] [PubMed]
34. Li, W.; Li, Y.; Song, Z.; Wang, Y.-X.; Hu, W. PEDOT-based stretchable optoelectronic materials and devices for bioelectronic interfaces. *Chem. Soc. Rev.* **2024**, *53*, 10575–10603. [CrossRef] [PubMed]
35. Zhu, L.; Liu, Q.; Zhang, Y.; Sun, H.; Chen, S.; Liang, L.; An, S.; Yang, X.; Zang, L. Recent advances in the tunable Optoelectromagnetic properties of PEDOTs. *Molecules* **2025**, *30*, 179. [CrossRef] [PubMed]
36. Zhang, M.; Yuan, W.; Yao, B.; Li, C.; Shi, G. Solution-processed PEDOT: PSS/graphene composites as the electrocatalyst for oxygen reduction reaction. *ACS Appl. Mater. Interfaces* **2014**, *6*, 3587–3593. [CrossRef] [PubMed]
37. Ma, B.; Ruan, M.; Ruan, K.; Sun, Y.; Cao, B.; Liu, Z. Interfacial engineering of MXene@ PEDOT composite for high-efficiency photoelectrocatalytic water splitting. *J. Power Sources* **2026**, *663*, 238842. [CrossRef]
38. Baruah, B.; Biswas, R.; Deb, P. Hybrid 2D-1D nanostructure of NiO composited with PEDOT: PSS and rGO: Bifunctional electrocatalyst towards methanol oxidation and oxygen evolution reaction. *Int. J. Energy Res.* **2022**, *46*, 16394–16415. [CrossRef]
39. Narayanasamy, S.; Jayaprakash, J. Carbon cloth/nickel cobaltite ($NiCo_2O_4$)/polyaniline (PANI) composite electrodes: Preparation, characterization, and application in microbial fuel cells. *Fuel* **2021**, *301*, 121016. [CrossRef]
40. Ng, W.C.; Chong, M.N. Organic-inorganic p-type PEDOT: PSS/CuO/MoS_2 photocathode with in-built antipodal photogenerated holes and electrons transfer pathways for efficient solar-driven photoelectrochemical water splitting. *Sustain. Mater. Technol.* **2023**, *38*, e00749. [CrossRef]
41. Selvaganesh, S.V.; Mathiyarasu, J.; Phani, K.; Yegnaraman, V. Chemical synthesis of PEDOT–Au nanocomposite. *Nanoscale Res. Lett.* **2007**, *2*, 546. [CrossRef]
42. Elkholy, A.E.; Duignan, T.T.; Sun, X.; Zhao, X.S. Stable α-MoO_3 electrode with a widened electrochemical potential window for aqueous electrochemical capacitors. *ACS Appl. Energy Mater.* **2021**, *4*, 3210–3220. [CrossRef]
43. Li, T.; Wan, W.; Cao, Y.; Xu, J.; Chai, H. $Co_2P_2O_7$@ MoO_3/NF composite electrocatalysts by different phosphorus sources for efficient oxygen evolution reaction and overall water splitting. *Colloid Interface Sci. Commun.* **2023**, *55*, 100727. [CrossRef]
44. Jiang, H.; Yu, Y.; Duan, X.; Chen, P.; Wang, S.; Qiu, X.; Ye, L.; Tu, X. Heterostructured MoO_3 anchored defect-rich NiFe-LDH/NF as a robust self-supporting electrocatalyst for overall water splitting. *Small* **2024**, *20*, 2307797. [CrossRef] [PubMed]
45. Ghorui, U.K.; Show, B.; Roy, D.; Basak, A.; Adhikary, B.; Mondal, A. Strategically designed Pd-induced changes in alkaline hydrogen evolution reaction and oxygen evolution reaction performances of electrochemical water oxidation by the galvanically synthesized MoO_2/MoO_3 composite thin film. *ACS Appl. Mater. Interfaces* **2024**, *16*, 3460–3475. [CrossRef] [PubMed]
46. Kong, T.; Song, J.; Zhang, Y.; Lim, E.L.; Liu, X.; Tress, W.; Bi, D. A Newly Crosslinked-double Network PEDOT: PSS@ PEGDMA toward Highly-Efficient and Stable Tin-Lead Perovskite Solar Cells. *Small* **2023**, *19*, 2303159. [CrossRef] [PubMed]
47. Lien, S.-Y.; Lin, P.-C.; Chen, W.-R.; Liu, C.-H.; Lee, K.-W.; Wang, N.-F.; Huang, C.-J. The mechanism of PEDOT: PSS films with organic additives. *Crystals* **2022**, *12*, 1109. [CrossRef]
48. Mitraka, E.; Jafari, M.J.; Vagin, M.; Liu, X.; Fahlman, M.; Ederth, T.; Berggren, M.; Jonsson, M.; Crispin, X. Oxygen-induced doping on reduced PEDOT. *J. Mater. Chem. A* **2017**, *5*, 4404–4412. [CrossRef] [PubMed]
49. Du, F.-P.; Cao, N.-N.; Zhang, Y.-F.; Fu, P.; Wu, Y.-G.; Lin, Z.-D.; Shi, R.; Amini, A.; Cheng, C. PEDOT: PSS/graphene quantum dots films with enhanced thermoelectric properties via strong interfacial interaction and phase separation. *Sci. Rep.* **2018**, *8*, 6441. [CrossRef] [PubMed]
50. Ouyang, L.; Musumeci, C.; Jafari, M.J.; Ederth, T.; Inganas, O. Imaging the phase separation between PEDOT and polyelectrolytes during processing of highly conductive PEDOT: PSS films. *ACS Appl. Mater. Interfaces* **2015**, *7*, 19764–19773. [CrossRef] [PubMed]
51. Jin Bae, E.; Hun Kang, Y.; Jang, K.-S.; Yun Cho, S. Enhancement of thermoelectric properties of PEDOT: PSS and tellurium-PEDOT: PSS hybrid composites by simple chemical treatment. *Sci. Rep.* **2016**, *6*, 18805. [CrossRef] [PubMed]
52. Yu, M.; Budiyanto, E.; Tüysüz, H. Principles of water electrolysis and recent progress in cobalt-, nickel-, and iron-based oxides for the oxygen evolution reaction. *Angew. Chem. Int. Ed.* **2022**, *61*, e202103824. [CrossRef] [PubMed]
53. Zhai, Y.; Ren, X.; Sun, Y.; Li, D.; Wang, B.; Liu, S.F. Synergistic effect of multiple vacancies to induce lattice oxygen redox in NiFe-layered double hydroxide OER catalysts. *Appl. Catal. B Environ.* **2023**, *323*, 122091. [CrossRef]
54. Hanan, A.; Shu, D.; Aftab, U.; Cao, D.; Laghari, A.J.; Solangi, M.Y.; Abro, M.I.; Nafady, A.; Vigolo, B.; Tahira, A. Co_2FeO_4@ rGO composite: Towards trifunctional water splitting in alkaline media. *Int. J. Hydrogen Energy* **2022**, *47*, 33919–33937. [CrossRef]
55. Tang, C.; Zhong, L.; Xiong, R.; Xiao, Y.; Cheng, B.; Lei, S. Regulable in-situ autoredox for anchoring synergistic Ni/NiO nanoparticles on reduced graphene oxide with boosted alkaline electrocatalytic oxygen evolution. *J. Colloid Interface Sci.* **2023**, *648*, 181–192. [CrossRef] [PubMed]
56. Ma, L.; Sui, S.; Zhai, Y. Preparation and characterization of Ir/TiC catalyst for oxygen evolution. *J. Power Sources* **2008**, *177*, 470–477. [CrossRef]

57. Guo, C.; Sun, X.; Kuang, X.; Gao, L.; Zhao, M.; Qu, L.; Zhang, Y.; Wu, D.; Ren, X.; Wei, Q. Amorphous Co-doped MoO_x nanospheres with a core–shell structure toward an effective oxygen evolution reaction. *J. Mater. Chem. A* **2019**, *7*, 1005–1012. [CrossRef]
58. Rani, B.J.; Ravi, G.; Yuvakkumar, R.; Ameen, F.; AlNadhari, S.; Hong, S. Fabrication and electrochemical OER activity of Ag doped MoO_3 nanorods. *Mater. Sci. Semicond. Process.* **2020**, *107*, 104818. [CrossRef]
59. Shaik, B.; Dharman, R.K.; Oh, T.H. $Cu(OH)_2$@ MoO_3 Nanorod Heterostructure for Efficient Overall Electrocatalytic Water Splitting in an Alkaline Medium. *Langmuir* **2026**, *42*, 6091–6100. [CrossRef] [PubMed]
60. Dhanabalan, K.; Bhosale, M.; Sriram, G.; Sadhasivam, T.; Oh, T.H. An Investigation of the Interface between Transition Metal Oxides (MnO_x, FeO_x, CoO_x and NiO_x)/MoO_3 Composite Electrocatalysts for Oxygen Evolution Reactions. *Inorganics* **2024**, *12*, 241. [CrossRef]
61. Cogal, S.; Cogal, G.C.; Mičušík, M.; Michalcova, A.; Šlouf, M.; Omastová, M. Conducting polymer-templated and nonnoble metal doped $MoSe_2$ hybrids as bifunctional electrocatalysts for overall water splitting. *J. Electroanal. Chem.* **2023**, *946*, 117728. [CrossRef]
62. Singh, A.; Singh, A.; Kociok-Köhn, G.; Bhimireddi, R.; Singh, A.; Singh, A.K.; Kumar, A.; Muddassir, M. Ternary copper molybdenum sulfide (Cu_2MoS_4) nanoparticles anchored on PANI/rGO as electrocatalysts for oxygen evolution reaction (OER). *Appl. Organomet. Chem.* **2022**, *36*, e6683. [CrossRef]
63. Lingappan, N.; Jeon, I.; Lee, W. Polyaniline induced multi-functionalities in interfacially coupled electrocatalysts for hydrogen/oxygen evolution reactions. *J. Mater. Chem. A* **2023**, *11*, 17797–17809. [CrossRef]
64. Liu, Y.; Li, J.; Li, F.; Li, W.; Yang, H.; Zhang, X.; Liu, Y.; Ma, J. A facile preparation of $CoFe_2O_4$ nanoparticles on polyaniline-functionalised carbon nanotubes as enhanced catalysts for the oxygen evolution reaction. *J. Mater. Chem. A* **2016**, *4*, 4472–4478. [CrossRef]
65. Farid, M.F.; Rehman, M.U.U.; Rehman, J.U.; Sajjad, W.; Fazal, M.W.; Khan, M.A.; Akhtar, N. In situ synthesis of manganese oxide/iron oxide/polyaniline composite catalyst for oxygen evolution reaction. *J. Mater. Res.* **2024**, *39*, 981–991. [CrossRef]
66. Alharthy, M.; Suliman, M.H.; Al-Betar, A.-R.; Wang, Y.; Tian, Z.; Drmosh, Q.A.; Yamani, Z.H.; Qamar, M. Reaping the catalytic benefits of both surface ($NiFe_2O_4$) and underneath (Ni_3Fe) layers for the oxygen evolution reaction. *Sustain. Energy Fuels* **2021**, *5*, 2704–2714. [CrossRef]
67. Brijesh, K.; Bindu, K.; Shanbhag, D.; Nagaraja, H. Chemically prepared Polypyrrole/$ZnWO_4$ nanocomposite electrodes for electrocatalytic water splitting. *Int. J. Hydrogen Energy* **2019**, *44*, 757–767. [CrossRef]
68. Jia, X.; Gao, S.; Liu, T.; Li, D.; Tang, P.; Feng, Y. Fabrication and bifunctional electrocatalytic performance of ternary CoNiMn layered double hydroxides/polypyrrole/reduced graphene oxide composite for oxygen reduction and evolution reactions. *Electrochim. Acta* **2017**, *245*, 59–68. [CrossRef]
69. Chinnappan, A.; Bandal, H.; Ramakrishna, S.; Kim, H. Facile synthesis of polypyrrole/ionic liquid nanoparticles and use as an electrocatalyst for oxygen evolution reaction. *Chem. Eng. J.* **2018**, *335*, 215–220. [CrossRef]

Disclaimer/Publisher's Note: The statements, opinions and data contained in all publications are solely those of the individual author(s) and contributor(s) and not of MDPI and/or the editor(s). MDPI and/or the editor(s) disclaim responsibility for any injury to people or property resulting from any ideas, methods, instructions or products referred to in the content.